



Seasonal trends in the wintertime photochemical regime of the Uinta Basin, Utah, USA

Marc L. Mansfield and Seth N. Lyman

Department of Chemistry and Biochemistry, Utah State University Uinta Basin, Vernal, UT 84078, USA

Correspondence: Marc L. Mansfield (marc.mansfield@usu.edu)

Received: 8 October 2024 – Discussion started: 5 November 2024

Revised: 17 May 2025 – Accepted: 19 May 2025 – Published: 25 September 2025

Abstract. Several lines of evidence indicate that the photochemical regime, i.e., the degree to which ozone production is either VOC- or NO_x -limited, varies with season in the Northern Hemisphere. For most regions, the question is patently academic, since excessive ozone occurs only in summer. However, the Uinta Basin in Utah, USA, exhibits ozone in excess of regulatory standards in both winter and summer. We have performed extensive Framework for 0-D Atmospheric Modeling (F0AM) box modeling to better understand these trends. The models indicate that, in late December, the Basin's ozone system is VOC-sensitive and either NO_x -insensitive or NO_x -saturated. Sensitivity to NO_x grows throughout the winter, and, in early March, the system is about equally sensitive to VOC and NO_x . The main driver for this trend is the increase in available solar energy as indicated by the noontime solar zenith angle (SZA). A secondary driver is a decrease in precursor concentrations throughout the winter, which decrease because of, firstly, a dilution effect as thermal inversions weaken and, secondly, an emission effect because certain emission sources are stronger at colder temperatures. On the other hand, temperature and absolute humidity (AH) are not important direct drivers of the trend.

1 Introduction

The Uinta Basin of Utah and the Upper Green River Basin of Wyoming are the only locations worldwide with documented high wintertime concentrations of ozone that consistently exceed 70 ppb. This unique atmospheric phenomenon results because both basins are prone to multi-day, persistent wintertime thermal inversions which trap ozone precursors in a tight boundary layer. A high surface albedo resulting from snow cover is also required (Schnell et al., 2009). Both basins are rural but are home to an active oil and natural gas extraction industry, which accounts for a major share of wintertime atmospheric emissions (Lyman et al., 2013, 2018; Edwards et al., 2014). Interestingly, many urban valleys and basins have inversions and snow cover, but, if anything, they are NO_x -saturated and titrate out ozone in winter (Shah et al., 2020; Li et al., 2021). The preferred explanation for the phenomenon is that the precursor speciation unique to the oil and gas industry is well suited for winter ozone production (Schnell et al., 2009; Edwards et al., 2014; Ahmadov et al., 2015; Matichuk et al., 2017; Mansfield and Hall, 2018).

Knowledge of the photochemical regime, or the degree to which an ozone system is either NO_x - or VOC-sensitive, is important in efforts to control ozone concentrations. The photochemical regime is controlled by the ratio of VOC to NO_x , but the ratio dividing the NO_x - and VOC-sensitive regimes varies with VOC reactivity, meteorology, and other factors (Sillman, 1999). This ratio determines the relative supply and fate of the radicals that catalyze ozone production. VOC-sensitive regimes are characterized by low radical concentration (including OH, HO_2 , and organic peroxy radicals) relative to NO_x , whereas NO_x -sensitive regimes represent the opposite scenario (Sillman et al., 1999). Ozone production depends on VOC in these regimes because an increase in VOC will lead to more VOC-dependent radical propagation reactions that allow more ozone formation. In the opposite case, adequate radicals exist, but low NO_x concentrations reduce the availability of O from NO_2 photolysis, which reacts with O_2 to create O_3 . In a low- NO_x environment (i.e., NO_x -sensitive), radical quenching will tend to occur via self-reaction, generating hydrogen peroxide (HOOH)

and other peroxides, whereas, in a high- NO_x environment (i.e., VOC-sensitive), radical quenching will tend to occur via reaction with NO_x , generating nitric acid and other reactive nitrogen species (Peng et al., 2011).

It is well known that the ozone production efficiency, i.e., the number of ozone molecules generated for each NO_x molecule consumed (defined operationally as the slope of the least-squares trend line of O_3 vs. NO_z concentrations, where $\text{O}_3 = \text{O}_3 + \text{NO}_2$, $\text{NO}_z = \text{NO}_y - \text{NO}_x$, and NO_y = all reactive nitrogen compounds), indicates the relative photochemical regime, with larger values indicating a shift towards relatively higher NO_x sensitivity and vice versa (Sillman, 1995, 1999; Sillman et al., 1997, 1998; Rickard et al., 2002; Sillman and He, 2002; Seinfeld and Pandis, 2006; Chou et al., 2009; Mazzuca et al., 2016). Another photochemical indicator with the advantage that it can be determined from satellite measurements is the ratio of the column densities of HCHO and NO_2 . Larger values of the column HCHO/ NO_2 ratio also indicate a shift towards NO_x sensitivity (Tonnesen and Dennis, 2000; Martin et al., 2004; Duncan et al., 2010; Choi et al., 2012; Jin et al., 2017).

In many regions of North America, Europe, and East Asia, studies based on models or on measurements of photochemical indicators have observed seasonal trends in the photochemical regime. It is common to see ozone systems that are more NO_x -sensitive in summer and more VOC-sensitive in winter (Kleinman, 1991; Jacob et al., 1995; Liang et al., 1998; Martin et al., 2004; Jin et al., 2017). In this paper, we report a similar trend in the Uinta Basin, Utah, USA. For most regions, the question of winter vs. summer ozone chemistry is purely academic because ozone concentrations in exceedance of regulatory limits only occur in summer. However, in the Uinta Basin, exceedances occur in winter and summer. Therefore, an understanding of the transition takes on added importance.

Below, we report box model calculations to determine the drivers for this trend and to estimate sensitivities to NO_x and VOC throughout the winter. The models indicate that, in early winter, the Basin is either VOC-sensitive or NO_x -saturated (in the more restrictive sense of these terms, as defined below at the end of Sect. 2.5), while, in late winter, NO_x and VOC sensitivities are about the same. We show that the main drivers for the trend are the change in solar zenith angle (SZA) and a decrease in average precursor concentrations over the course of the winter. Other meteorological trends, specifically mean temperature and mean absolute humidity (AH), are not important drivers. We also consider the factors driving the decrease in precursor concentrations. The data support a dilution effect as inversions become less intense during the advancing season. There is also evidence for an emission effect: certain emission classes, such as engine efficiency or equipment used more frequently in cold weather, are linked directly or indirectly to the temperature. This improved knowledge of the Basin's photochemical regime allows us to suggest possible ozone abatement strategies.

Edwards et al. (2014) have also published box-model results for the Uinta Basin in winter. An important difference between their model and ours is that we employ a VOC speciation based on a more recent, exhaustive measurement set (Lyman et al., 2021). Our speciation profile is reported below.

2 Methodology

2.1 Atmospheric measurements

Measurements used to construct the VOC speciation profile were collected at the Horsepool monitoring station in central Uintah County, Utah, USA (Fig. 1). Ozone was measured with an Ecotech Model 9810 analyzer. A Thermo 42i was used to measure NO , true NO_2 (via an Air Quality Design photolytic converter), and NO_y (via a heated molybdenum oxide converter). NO_z was determined as the difference between NO_y and NO_x . 3 h averages of whole-air samples were routinely collected in Silonite-coated stainless canisters, and organic compounds were preconcentrated from the canisters in the laboratory by cold-trap dehydration using an Entech 7200 and analyzed by gas chromatography and flame ionization detection (compounds with two and three carbons) and mass spectrometry (all other compounds). Additional details are given in Mansfield and Lyman (2021) and Lyman et al. (2021).

2.2 Photochemical indicators in the Uinta Basin

The Uinta Basin is a structural and sedimentary basin in eastern Utah, Fig. 1, that produces oil and natural gas. Unless stated otherwise, the data and models discussed here are from the Horsepool monitoring station at latitude 40.1434° and longitude -109.4689° . Figure 2 displays the ozone production efficiency, calculated daily as the slope of the least-squares trend lines of O_3 vs. NO_z and then averaged. Figure 3 displays the mean ratio of column HCHO data to tropospheric column NO_2 data obtained from the Ozone Monitoring Instrument (OMI; NASA-OMI, 2022). The threshold between VOC and NO_x sensitivity is near 1 or 2 for both indicators, but the precise threshold depends on local conditions, and it is best to interpret the indicators in light of modeling results, as we do below. Nevertheless, the data indicate a seasonal trend, with the system tending towards VOC sensitivity in early winter and NO_x sensitivity in late winter.

2.3 Trends in meteorological variables and precursor concentrations

Any property that varies systematically through the season might conceivably be a driver for the trend in photochemical indicators seen in Figs. 2 and 3. This could include the actinic flux, the ambient absolute humidity, and the ambient temperature. Here, we take the noontime solar zenith angle as

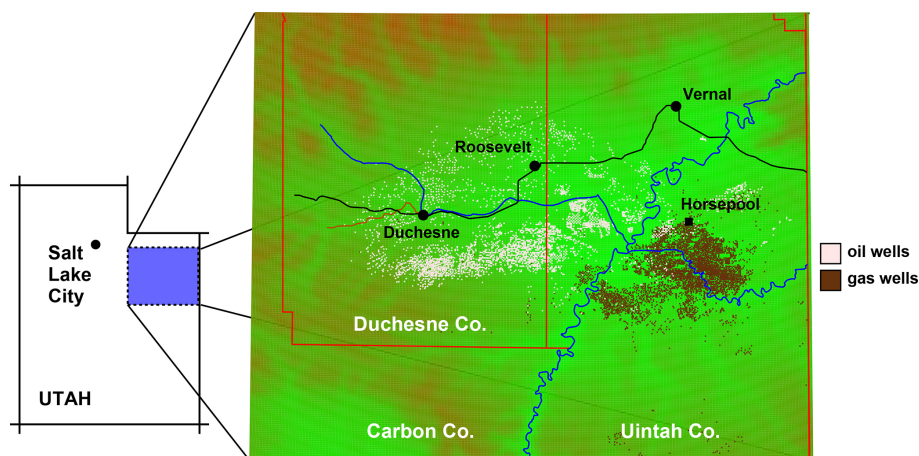


Figure 1. Map of the Uinta Basin. Duchesne, Roosevelt, and Vernal are major population centers. The Horsepool monitoring station and the distribution of oil and natural gas wells are also shown.

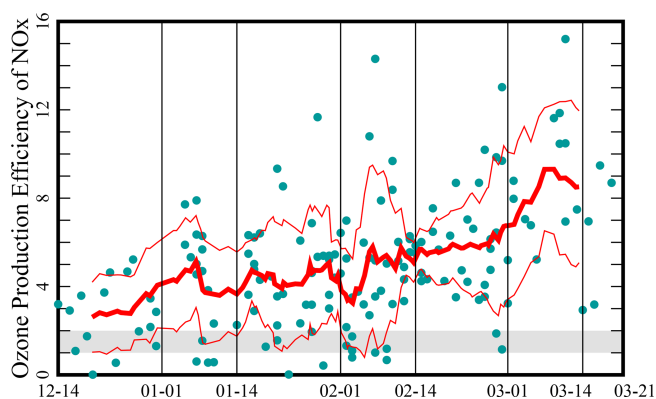


Figure 2. Ozone production efficiency at the Horsepool monitoring station in the Uinta Basin. Data from days when the hourly ozone concentration exceeded 60 ppb from 2011 to 2022 and from December to March are shown. The red traces show 10-point running averages plus or minus 1 standard deviation. The threshold between VOC and NO_x sensitivity occurs around 1 or 2 and appears in gray.

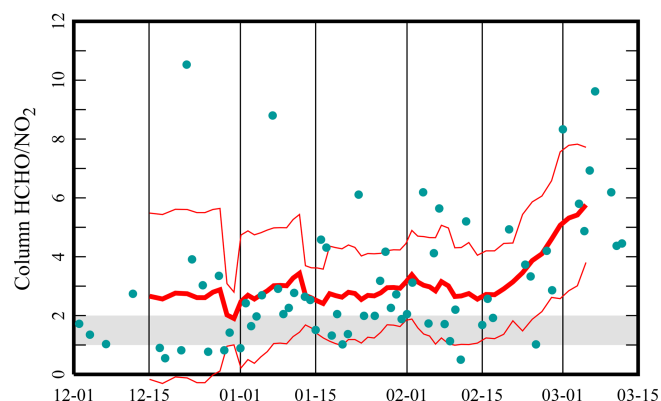


Figure 3. Mean ratio of column HCHO to tropospheric column NO_2 from the Ozone Monitoring Instrument (OMI) pixel that contains the Horsepool station, on the indicated date, including all available data from 2009 to 2020 and between 1 December and 15 March. The red traces show 10-point running averages plus or minus 1 standard deviation. The threshold between VOC and NO_x sensitivity occurs around 1 or 2 and appears in gray.

a proxy for the actinic flux. This is permissible because, during high-ozone episodes, the sky is typically free of clouds and surface albedo contributed by snow cover is essentially uniform. The noontime solar zenith angle is given to a good approximation by the formula

$$\theta = L + D \cos(\omega_E t), \quad (1)$$

where L is the latitude (40.14° at the Horsepool station), D is the tilt of Earth's axis (23.44°), ω_E is the angular frequency of Earth's revolution ($2\pi \text{ y}^{-1}$), and t is the time elapsed since the last winter solstice (Finlayson-Pitts and Pitts, 2000). Therefore, between the winter solstice and the vernal equinox, θ varies from about 63.6 to 40.1° . Figure 4 displays temperature and absolute humidity trends at the Horsepool station. Daily averages of temperature and abso-

lute humidity between the hours of 11:00 and 20:00 MST, on dates from 15 December to 15 March and years between 2012 and 2021, are shown (the rationale for computing means between the hours of 11:00 and 20:00 MST will be explained in Sect. 3, Calculation 4). Throughout this work, the winter season has been divided into 6 fortnights or half-months, defined in Fig. 4. The fortnights will be designated “late December”, “early January”, and so on. Absolute humidity was calculated from measured values of temperature and relative humidity using a standard formula for the temperature dependence of the saturation vapor pressure of water (Seinfeld and Pandis, 2006).

NO_x and methane concentrations are measured continuously at Horsepool during winter months, but non-methane

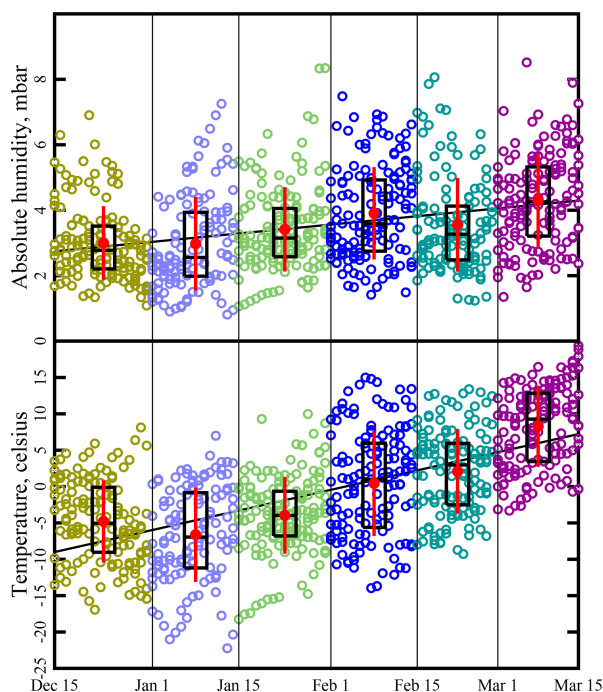


Figure 4. Absolute humidity and temperature trends throughout the winter. Humidity and temperature data are from the Horsepool monitoring station. Straight lines are the least-squares trend lines through the data points. Data are binned into 6 fortnights: late December, early January, etc. Black boxes show the 25th, 50th, and 75th percentiles. Red dots and whiskers show the mean plus or minus 1 standard deviation.

organics are not. Therefore, we take methane as a marker for VOC concentrations, employing the conversion factor, explained below, of 0.0619 mol non-methane VOC for each mole of methane. Figure 5 indicates that NO_x and methane concentrations are lower in late winter.

The available data indicate that a dilution effect caused by weakening inversions contributes to the systematic decrease in precursor concentrations. Tethersonde measurements do not occur on a regular basis in the Uinta Basin, so we rely on the correlation between surface temperature and altitude to obtain a quantitative measure of inversion strength (Mansfield and Hall, 2013, 2018). A similar approach has been adopted by other authors (Whiteman et al., 2004; Largeron and Staquet, 2016). We define the daily “pseudo-lapse rate”, Ψ , in terms of the slope of the least-squares trend line of the daily maximum surface temperature vs. altitude at a number of sites:

$$\Psi = -\frac{\partial T}{\partial z}. \quad (2)$$

To exclude points that often lie in the non-linear region of the temperature–altitude profile, we only include sites between 1400 m a.s.l. (the floor of the Basin) and 2000 m a.s.l. (Mansfield and Hall, 2013, 2018). The daily maximum temperature is used to focus on multi-day, persistent, as opposed to

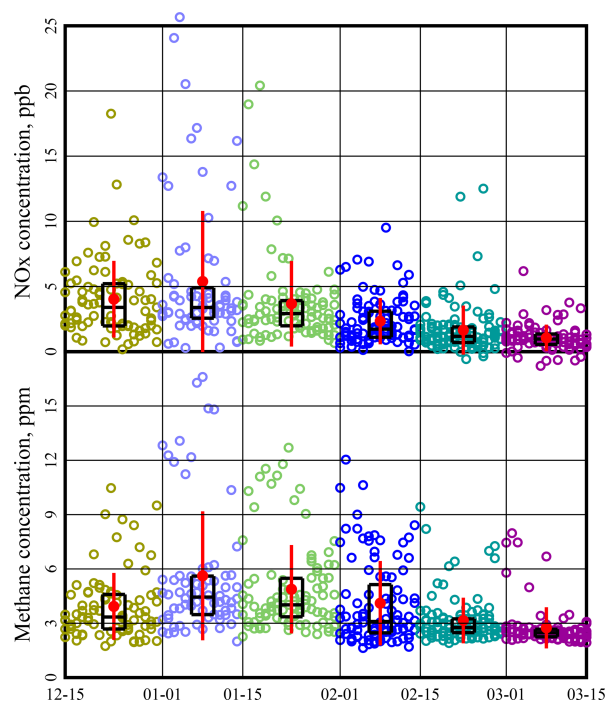


Figure 5. Average daily NO_x and CH_4 concentrations measured at Horsepool. Each symbol is a daily average taken over the hours 11:00 to 20:00 MST. Only days when both NO_x and CH_4 data were reported have been displayed. Black boxes show the 25th, 50th, and 75th percentiles. Red dots and whiskers show the mean plus or minus 1 standard deviation.

diurnal, inversions. Low values of Ψ indicate strong inversions with tight boundary layers, while high values indicate a well-mixed boundary layer. Figure 6 shows the variation in Ψ as the season progresses. Inversions are seen to be more intense in early winter. Figure S25 in the Supplement shows the correlation between precursor concentrations and Ψ , and Fig. S26 shows the correlation between CH_4 and NO_x concentrations. These correlations all confirm that precursors are more diluted late in the season because the mixing layer is deeper.

However, emission effects might also contribute to the seasonal decline in precursor concentrations. Many studies find that vehicular NO_x emissions are greater in winter. Several causative factors are mentioned, including poorer engine performance in the cold, cold starts, and operation of NO_x after-treatment systems (e.g., catalytic converters) outside their optimal temperature range (Dardiotis et al., 2013; Reiter and Kockelman, 2016; Saha et al., 2018; Suarez-Bertoa and Astorga, 2018; Grange et al., 2019; Weber et al., 2019; Hall et al., 2020; Li et al., 2020; Wang et al., 2020; Bishop et al., 2022; Wærsted et al., 2022). Most studies agree that the effect is present in light- and heavy-duty diesel vehicles (the predominant form of transportation near Horsepool), while studies investigating the effect in gasoline vehicles give conflicting results, perhaps because of differences in NO_x after-

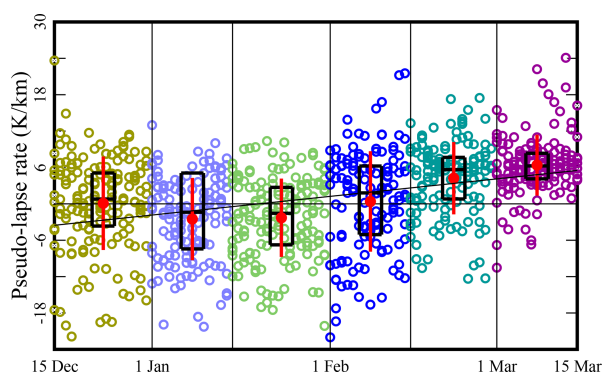


Figure 6. Variation in pseudo-lapse rate Ψ as the season progresses. Each symbol represents the calculation for 1 d. Black boxes indicate the 25th, 50th, and 75th percentiles. Red dots and whiskers display the mean plus or minus 1 standard deviation.

treatment systems (Dardiotis et al., 2013; Suarez-Bertoa and Astorga, 2018; Grange et al., 2019; Li et al., 2020). Wærsted et al. (2022) report vehicular NO_x emissions to be about a factor of 3 larger at -12°C than at $+12^\circ\text{C}$ in Norway. Hall et al. (2020) report that vehicular NO_x emissions in the Baltimore–Washington (USA) metropolitan area are about twice as large at -5°C than at 25°C . Other studies give smaller ratios between summer and winter. Such variability likely results from variations in the composition of the local fleet (e.g., gasoline vs. diesel engines and older vs. newer NO_x after-treatment systems). The Uinta Basin is also home to other NO_x sources, such as well-site and portable natural gas-fueled heaters, that operate only in winter. We have been unable to find data on temperature trends in the NO_x emissions from drilling rigs, but these may behave similarly to diesel-powered vehicles. Hence, it is likely that dilution and emission effects both contribute to the decrease in NO_x concentrations. This seasonal trend in NO_x concentrations obviously deserves more study.

Figure 5 indicates that methane concentrations also vary systematically as the season progresses. Any dilution effects, cited above, will similarly affect methane concentrations. However, emissions correlated with ambient temperature may also contribute, for example, from equipment such as glycol dehydrators, heat trace pumps, and “hot oil” trucks and from operations to thaw frozen lines, including pipeline venting and well blowdowns. Like NO_x , this methane trend also deserves further study.

Note that methane concentrations are rarely below 2 ppm; i.e., in late winter, they approach but never fall below the global background concentration (NOAA, 2022). This is additional evidence of a well-mixed boundary layer under certain conditions.

2.4 Box modeling procedures

We used the “Framework for 0-D Atmospheric Modeling” (F0AM) platform, version 4.2.1, in a configuration similar to Lyman et al. (2022), which has been coded as MATLAB script (Wolfe et al., 2016). A subset of the “Master Chemical Mechanism” (MCM), v3.3.1, served as the chemistry mechanism (Jenkin et al., 2003, 2015; Saunders et al., 2003; Zong et al., 2018; MCM, 2022). Descriptions of all other input variables are summarized in Tables 1 and 2. The VOC speciation profile appearing in Table 2 was assigned using measurements from the Horsepool measuring station reported by Lyman et al. (2021). The same speciation profile was also used in Lyman et al. (2022). Obviously, use of the same organic speciation profile throughout our study means that we were unable to capture its spatial and temporal variations and any impacts that such variations would have on the ability of the models to produce secondary radicals. Nevertheless, since the speciation was derived from measurements at Horsepool, we believe it faithfully represents the ambient organic concentrations in this oil- and gas-producing region. Representative MATLAB code and input files are included in the Supplement. Each simulation spanned 4 d, including 3 d of spin-up. According to Table 2, one VOC unit is equivalent to 4920 ppb of methane and 304.4 ppb of the non-methane hydrocarbons, alcohols, and carbonyl compounds listed there.

Often, we wanted to compare two models with the same absolute humidity profile but at different temperatures. To change the temperature without changing the absolute humidity of course requires an adjustment of the relative humidity.

2.5 Definition of sensitivity

Let x represent some independent variable in the model, for example, the concentration of a precursor, and let y represent a dependent variable, which for our purposes is almost always the maximum ozone concentration on day four of a simulation run. A small variation in the independent variable, dx , induces a change, dy , in the dependent variable. The fractional changes in the two variables are dx/x and dy/y . We define the sensitivity, S , of the dependent variable on the independent variable as the ratio of these two fractional changes:

$$S = \left(\frac{dy}{y} \right) / \left(\frac{dx}{x} \right) = \frac{x}{y} \frac{dy}{dx} = \frac{d \ln y}{d \ln x}. \quad (3)$$

A small, e.g., 1 %, change in x produces an S % change in y . By this definition, S is unitless and is the slope of the tangent on a log–log plot. When the independent variable is the NO_x or VOC concentration, we will use the notation S_{NO_x} and S_{VOC} , respectively. S values were calculated by numerical differentiation using three separate runs at x and $x \pm dx$ for dx on the order of a few percent. We use the phrases “ NO_x -

Table 1. Inputs to the box models.

Variable	Comments	Assigned value
VOC concentrations	Speciation profile from Table 2. One “unit” of input VOC implies the 59 compounds at the indicated concentrations. In any run, the total VOC concentration was set by scaling the total number of VOC “units”. Species concentrations were held constant throughout the run (LinkSteps = 1, HoldMe = 1), equivalent to assuming VOC concentrations are at steady state with emission, deposition, and chemical transformation in balance.	One VOC unit = 4920 ppb CH ₄ + 304.4 ppb of non-methane organics.
NO _x concentrations	“Family conservation” option switched on; NO _x = NO + NO ₂ concentrations held constant throughout each hour. Hourly NO and NO ₂ profiles prepared in several ways: (1) observational data from a single day, (2) averages of observational data from a number of days, (3) rescaling any of the profiles prepared by the previous two ways.	
Background ozone	Lyman et al. (2013, 2018)	50 ppb
Temperature	Hourly data from a given day.	
Relative humidity	Hourly data from a given day.	
Barometric pressure	Hourly data from a given day.	Average over all models: 845 ± 7 (1σ) mbar.
CO concentration	Hourly concentration measurements from Horsepool on 27 February 2019*. CO concentration held constant throughout each hour (LinkSteps = 1, HoldMe = 1).	272 ppb (average from 11:00 to 20:00 MST)
<i>k</i> _{dil} , dilution factor	Same as Edwards et al. (2014).	1.8 × 10 ^{−5} Hz: daylight; 2.0 × 10 ^{−6} Hz: dark
Solar zenith angle	Computed with the F0AM procedure sun_position from the time, date, latitude, longitude, and elevation at Horsepool.	
Albedo	Typical of snow surfaces at Horsepool.	0.7
Ozone column	From the NASA Giovanni website (NASA Giovanni, 2022).	275 DU
<i>J</i> _{corr}	Correction factor for scaling <i>J</i> values (Wolfe et al., 2016).	0.5

* Due to an oversight, CO concentration data from 27 February 2019 were applied in all modeling runs. However, we verified that modeled ozone concentrations changed by no more than about 1 ppb even when we completely zeroed out the CO concentration.

saturated” to indicate $S_{\text{VOC}} > 0 > S_{\text{NO}_x}$, “VOC-sensitive” to indicate $S_{\text{VOC}} > S_{\text{NO}_x} > 0$, and “NO_x-sensitive” to indicate $S_{\text{NO}_x} > S_{\text{VOC}} > 0$.

3 Results

We performed five separate calculations to probe the effect of the systematic variations documented in Sect. 2.3.

3.1 Calculation 1. NO_x and VOC sensitivity of 24 different models

We identified 24 multi-day inversion episodes with high ozone between 15 December and 15 March and between 2013 and 2021. Typically, ozone concentrations in the Basin grow for a number of days during a multi-day inversion episode, peaking the day before the inversion breaks (Lyman et al., 2013, 2018). Maximum 1 h ozone concentrations

on these days varied anywhere from 59 to 154 ppb. Observational values of meteorological data and of NO_x concentrations were employed as input data. Input VOC concentrations were in the proportion given in Table 2. For each model, we defined a “base case” using the observed NO_x concentrations and by scaling the input VOC concentration until the maximum day-four ozone concentration agreed with the peak ozone measurement. These 24 models are summarized in Table 3 and are identified by the date of maximum ozone. Figure 7 shows how the VOC and NO_x sensitivities of each of the base-case models vary throughout the season. In December and January, VOC sensitivities are always larger than NO_x sensitivities, and NO_x sensitivities are often negative. In late winter, NO_x and VOC sensitivities are typically comparable. The three late-winter base-case models (27 February 2019, 3 March 2013, 6 March 2019) have nearly equal sensitivities to NO_x and VOC.

Table 2. VOC concentrations in the F0AM box model (Lyman et al., 2021). The concentrations listed here constitute one “unit” of VOC in the models.

Methane		Total	Aromatics		Total
Methane	4920.0 ppb	4920.0 ppb	Benzene	1.2 ppb	3.0 ppb
Non-methane alkanes		Total	Toluene	1.2	
Ethane	123.0 ppb	264.8 ppb	<i>o</i> -Xylene	0.1	
Propane	63.0		<i>m</i> -Xylene	0.2	
<i>n</i> -Butane	25.0		<i>p</i> -Xylene	0.1	
Isobutane	15.0		Ethylbenzene	0.1	
<i>n</i> -Pentane	10.0		1,2,3-Trimethylbenzene	0.1	
Isopentane	11.0		<i>n</i> -Propyl benzene	0	
<i>n</i> -Hexane	4.0		Isopropyl benzene	0	
2-Methylpentane	3.0		1,2,4-Trimethylbenzene	0	
3-Methylpentane	2.0		1,3,5-Trimethylbenzene	0	
2,2-Dimethylbutane	0.3		1-Ethyl-2-methylbenzene	0	
2,3-Dimethylbutane	1.6		1-Ethyl-3-methylbenzene	0	
<i>n</i> -Heptane	1.9		1-Ethyl-4-methylbenzene	0	
2-Methylhexane	0.8		Styrene	0	
3-Methylhexane	1.2		Alcohols		Total
<i>n</i> -Octane	0.8		Methanol	10.0 ppb	12.6 ppb
<i>n</i> -Nonane	0.2		Ethanol	0.3	
<i>n</i> -Decane	0.2		Isopropanol	2.3	
Cyclohexane	1.8		Carbonyls		Total
Alkenes and alkynes		Total	Formaldehyde	6.5 ppb	21.0 ppb
Ethylene	1.1 ppb	3.0 ppb	Acetaldehyde	2.9	
Propylene	0.1		Butyraldehyde	1.3	
Acetylene	1.8		Acrolein	1.6	
1-Butene	0		Methacrolein	0.6	
<i>cis</i> -2-Butene	0		Benzaldehyde	4.4	
<i>trans</i> -2-Butene	0		Acetone	3.0	
1-Pentene	0		Methyl ethyl ketone	0.7	
<i>cis</i> -2-Pentene	0		Propionaldehyde	0	
<i>trans</i> -2-Pentene	0		Valeraldehyde	0	
1-Hexene	0		Crotonaldehyde	0	
			Cyclohexanone	0	

The late-winter convergence of S_{VOC} and S_{NO_x} appears to result more from an increase in S_{NO_x} than from a decrease in S_{VOC} . The trend line for S_{VOC} has a slope of -1.6σ , where σ is the standard deviation of the slope, and a p value of 0.13 from a Mann–Kendall trend test (Mann, 1945; Kendall, 1975). Therefore, the downward trend in S_{VOC} may be real, but our results lack sufficient statistical power to confirm this. On the other hand, with a slope of $+3.9\sigma$ and a very small Mann–Kendall p , the upward trend in S_{NO_x} is statistically significant.

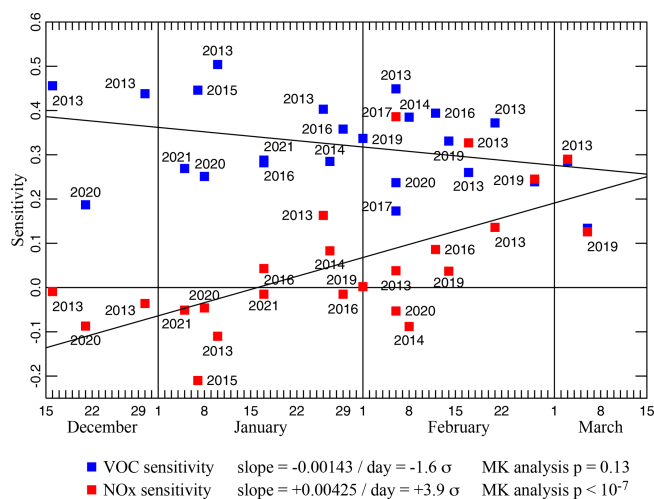
3.2 Calculation 2. Impact of changing meteorological and concentration variables

We examined five variables as candidate drivers for the change in photochemical regime documented above, namely,

VOC concentration, NO_x concentration, solar zenith angle (SZA), ambient temperature (T), and ambient absolute humidity (AH). Starting from one of the models in Table 3, we replaced just one of the above five variables with typical values from either an earlier or a later model. No other input quantity was varied. The solar zenith angle was varied by changing the date of the simulation. This lets us probe the effect of just one variable on S_{NO_x} and S_{VOC} . Figure 8 plots the change in sensitivity, ΔS_{NO_x} or ΔS_{VOC} , induced by the change in one of the five variables, solar zenith angle (ΔSZA), NO_x concentration (ΔNO_x), VOC concentration (ΔVOC), temperature (ΔT), and absolute humidity (ΔAH). For ease of interpretation, whenever one of the five variables trends downward during the winter (Eq. 1 and Figs. 4 and 5), the scale of the corresponding abscissa in Fig. 8 is

Table 3. List of FOAM models constructed.

Model	Date of peak ozone (yyyy-mm-dd)	Base-case concentrations		Mean temperature, °C	Mean absolute humidity, mbar
		VOC (multiples of Table 1)	NO _x , ppb (average between 11:00 and 20:00 MST)		
D13a	2013-12-16	2.25	7.04	−12.53	1.75
D20a	2020-12-21	0.30	4.91	−6.50	3.19
D13b	2013-12-30	1.6	6.24	−10.45	2.21
J21a	2021-01-05	0.5	3.41	−5.34	2.99
J15a	2015-01-07	0.9	13.07	+1.76	5.17
J20a	2020-01-08	0.45	3.32	−8.28	2.78
J13a	2013-01-10	1.7	12.05	−13.15	1.77
J16a	2016-01-17	0.65	2.83	+0.88	4.05
J21b	2021-01-17	0.5	2.81	−4.64	3.01
J13b	2013-01-26	2.5	4.62	−3.31	4.06
J14a	2014-01-27	0.75	2.47	−1.48	3.72
J16b	2016-01-29	0.65	3.51	−4.48	3.31
F19a	2019-02-01	0.60	2.74	−6.84	2.52
F13a	2013-02-06	1.3	4.65	−3.50	3.53
F17a	2017-02-06	4.00	0.76	+1.71	5.05
F20a	2020-02-06	0.25	2.73	−6.56	2.48
F14a	2014-02-08	0.5	4.56	+2.77	4.69
F16a	2016-02-12	1.00	3.18	+0.21	4.44
F19b	2019-02-14	0.55	2.87	−2.72	4.53
F13b	2013-02-17	2.4	1.81	−6.21	2.95
F13c	2013-02-21	1.05	3.14	−2.74	3.68
F19c	2019-02-27	0.85	1.35	−3.24	3.63
M13a	2013-03-03	1.55	2.29	+1.30	4.98
M19a	2019-03-06	0.15	1.12	−1.52	5.13

**Figure 7.** S_{VOC} and S_{NO_x} for 24 different box model runs. Slopes of the least-squares trend lines are given both as numerical values and as multiples of the standard deviations of the slopes. The p values from Mann–Kendall trend analyses are also shown.

shown in descending order. In this way, we see immediately whether modulating the variable tends to increase or decrease the sensitivity over the course of the winter. The scale of the ordinates in either row is identical, so the vertical displacement of each trend line indicates the relative strength of each individual driver. Most notably, the response to AH is very weak, indicating that absolute humidity is not an important driver. Traditionally, either the condition $|\text{slope}|/\sigma > 2$ or $p_{\text{MK}} < 0.05$ indicates a statistically significant trend in a data set. Therefore, of the eight remaining trends depicted in Fig. 8, the ΔS_{VOC} vs. ΔNO_x is least likely to be statistically significant. Normally, we expect each trend line to pass near the origin: a small change in only one variable usually leaves the model largely unchanged. The two trend lines relative to ΔNO_x fail to pass near the origin because the NO_x variable is defined as an average over a daily profile. Therefore, $\Delta \text{NO}_x = 0$ can occur even if the models are not equivalent. This also explains the greater scatter in the two ΔNO_x plots.

The total vertical displacement of each of the five drivers to the seasonal sensitivity trends. Trend lines in the temperature and absolute humidity plots are relatively flat, indicating that the solar zenith angle and the NO_x and VOC

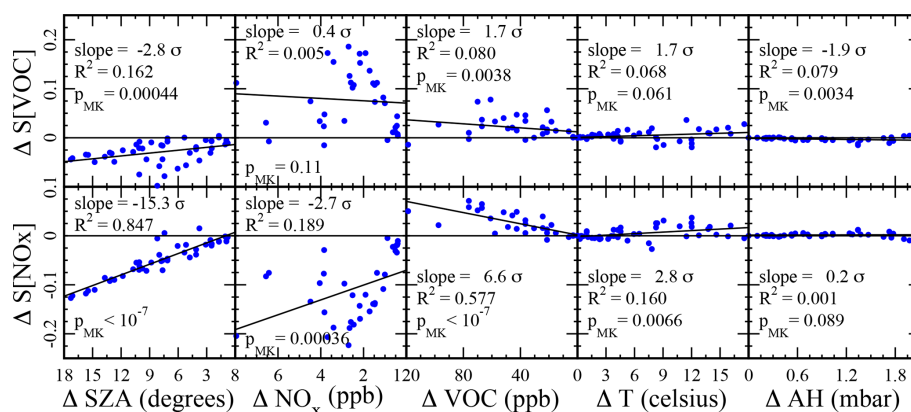


Figure 8. The change in sensitivity, ΔS_{NO_x} or ΔS_{VOC} , induced by the change in one of the five variables, solar zenith angle (ΔSZA), NO_x concentration (ΔNO_x), VOC concentration (ΔVOC), temperature (ΔT), and absolute humidity (ΔAH), for various models listed in Table 3. The scale on the abscissa appears in descending order if the corresponding variable trends downward during the winter. The slope of each trend line as a multiple of its standard deviation, the value of Pearson's R^2 , and the Mann–Kendall p value are shown for each data set.

Table 4. Vertical displacement of trend lines in Fig. 8.

Variable	ΔS_{VOC}	ΔS_{NO_x}
SZA	0.035 ± 0.012	0.131 ± 0.009
NO_x	-0.019 ± 0.046	0.121 ± 0.044
VOC	-0.025 ± 0.015	-0.068 ± 0.010
T	0.010 ± 0.006	0.019 ± 0.007
AH	-0.004 ± 0.002	0.0005 ± 0.0022
Total	-0.003 ± 0.050	0.20 ± 0.05

concentrations are the important drivers. Table 4 displays the values of all vertical displacements. Uncertainties were calculated from the standard deviations of the slopes. Sums of all five displacements are also tabulated. The uncertainty in the sums was calculated by propagating the uncertainties in each addend into the sum. The ΔS_{VOC} total is statistically zero, consistent with the finding that the S_{VOC} trend in Fig. 7 may not be statistically significant. The solar zenith angle and the NO_x concentration make comparable positive contributions to S_{NO_x} , while the VOC concentration makes a smaller negative contribution.

3.3 Calculation 3. Ozone isopleth diagrams

We calculated an ozone isopleth diagram for each of the 24 models in Table 3 by scaling NO_x and VOC concentrations relative to the base model. Each FOAM run required approximately 2 to 4 min on a MacBook Pro laptop, and generating the full diagram at high resolution proved to be too time-consuming. Rather, we calculated pixels at high resolution only around the boundary of the diagram and at 1/10 resolution throughout the interior. Pixels were also calculated at higher resolution in the vicinity of the “indicator curves”, to be defined below. The ozone isopleth surface at all remain-

ing pixels was generating by kriging interpolation (Kerry and Hawick, 1998). All 24 diagrams are given in the Supplement.

3.4 Calculation 4. Superposition of individual models to create ozone isopleth diagrams for each fortnight

According to Calculation 2, the only relevant variables are solar zenith angle and the precursor concentrations. This implies that all isopleth surfaces belonging to any one fortnight are approximately superposable. The VOC concentration unit, defined in reference to Table 2, is directly transferable between different models, but the NO_x concentration unit, defined in reference to the daily NO_x profile, is not. To test superposability, we assigned a different scale factor to the NO_x axis of each diagram and adjusted its value to optimize the superposition among all models from a given fortnight. We found that the scale factor for each model correlated best with the average NO_x concentration taken over the hours 11:00 to 20:00 MST and adopted this average to redefine the NO_x concentration axis on the ozone isopleth surfaces. For consistency, we have also used averages over the same hours, 11:00 to 20:00 MST, to report values of other variables.

Ozone isopleth surfaces for each of the 24 models listed in Table 3 were then superposed into six composite surfaces, one for each fortnight, and are shown in Fig. 9. All contributions defined at a given pixel on the original surfaces were averaged to estimate the ozone concentration in the composite pixel. Discontinuities in the contour curves occur because the diagrams of the individual models were not constructed with the same boundaries and because the individual models are not perfectly superposable. Nevertheless, the discontinuities are generally not large, validating the superposability assumption. The domains defined by the 25th and 75th percentiles in Figs. 4 and 5 appear in Fig. 9 as black rectangles and therefore define the domains at which precursor concen-

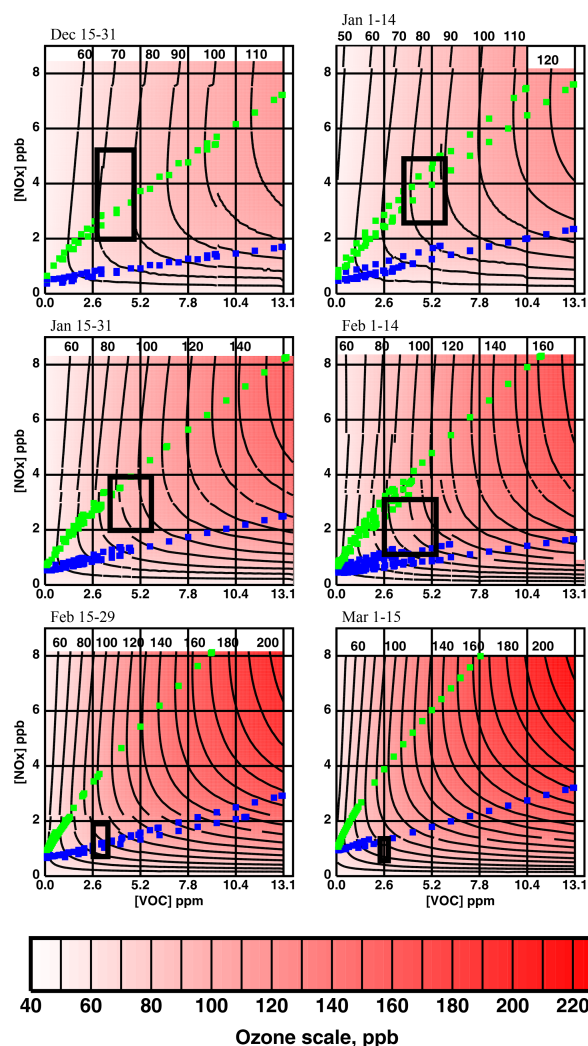


Figure 9. Composite ozone isopleth surfaces constructed from the 24 models listed in Table 3. Green squares define the locus of points at which $S_{\text{NO}_x} = 0$. Blue squares define the locus of points at which $S_{\text{NO}_x} = S_{\text{VOC}}$. Black rectangles were derived from the 25th–75th percentile boxes in Figs. 4 and 5 and therefore display the typical ranges of VOC and NO_x concentrations.

trations are at their typical values. The small green squares indicate points at which $S_{\text{NO}_x} = 0$. The small blue squares indicate points at which $S_{\text{NO}_x} = S_{\text{VOC}}$. These small squares define indicator curves: all points below the blue trace satisfy $S_{\text{NO}_x} > S_{\text{VOC}}$ and constitute the region of NO_x sensitivity. All points above the green trace satisfy $S_{\text{NO}_x} < 0$ and constitute the NO_x -saturation region. All points between the two traces satisfy $S_{\text{VOC}} > S_{\text{NO}_x} > 0$ and constitute the VOC-sensitive region. The indicator curves from each individual model are shown. The fact that these are all approximately superposable is further vindication of the superposability assumption.

3.5 Calculation 5. Impact of meteorology on ozone concentrations

It is obvious in Fig. 9 that, at any given value of VOC and NO_x concentrations, ozone concentration increases as the season progresses. Although our primary focus is seasonal trends in the photochemical regime, we have also performed box model calculations to analyze the trend in the ozone concentration itself. We have calculated temperature, absolute humidity, and noontime solar zenith angle sensitivities, S_T , S_{AH} , and S_θ , for the 24 models, obtaining the approximate ranges given in column 2 of Table 5. The third column summarizes the change in the variable over the course of the season and was extracted from Eq. (1) and Fig. 4. Column 4 gives the percentage change in the variable through the season. Multiplying columns 2 and 4 yields column 5, an estimate of the percentage change in ozone concentration induced by the change in each variable. All three variables exert a positive influence on ozone concentration. The predicted total change in ozone concentration is in the range of 40 % to 65 % from December to March. Contributions from temperature and absolute humidity are much weaker than from the solar zenith angle. We conclude that most of the increase in ozone concentration observed over the course of the winter at constant NO_x and VOC concentration is driven by the change in actinic flux.

Near the solstice, the solar zenith angle is insensitive to the date, so, to calculate S_θ , we modulated the latitude instead. The large value of S_θ helps explain the rarity of the winter ozone phenomenon. Apparently, it is only expected in a narrow range of latitudes. The Uinta and Upper Green River basins are at about the 40th and 42nd parallels, respectively. At just the 45th parallel, with a 12 % increase in noontime solar zenith angle relative to the Uinta Basin, we can expect ozone concentrations to decrease by about 13 % to 19 %. Therefore, we expect the oil and gas fields of Alberta and Alaska to be spared from winter ozone. Since snow cover is also required for winter ozone, we also expect it to be rare at lower latitudes (Mansfield and Hall, 2018). If global warming causes the snow line to drift farther north, high winter ozone concentrations may become rare even at the 40th to the 42nd parallel.

4 Discussion and conclusions

The trend in photochemical indicators documented in Figs. 2 and 3 is dominated more by an increase in NO_x sensitivity than a decrease in VOC sensitivity. S_{NO_x} increases from values below S_{VOC} and near zero, while S_{VOC} remains relatively flat. In the early season, S_{NO_x} is often negative.

Figure 9 demonstrates that two separate effects are responsible for the trend in photochemical indicators documented in Figs. 2 and 3.

Firstly, meteorological drivers dominated by the solar zenith angle push the indicator curves to higher levels as

Table 5. Sensitivities of ozone concentrations to noontime solar zenith angle (θ), temperature (T), and absolute humidity (AH).

$x =$	Range of S_x (25th to 75th percentile)	Range of x	% change in x from December to March	% change in $[O_3]$ from December to March
θ	−1.1 to −1.6	64 to 42°	−33 %	36 % to 53 %
T	0.25 to 0.65	263 to 279 K	16 %	4 % to 10 %
AH	0.02 to 0.04	2.7 to 4.2 mbar	56 %	1 % to 2 %

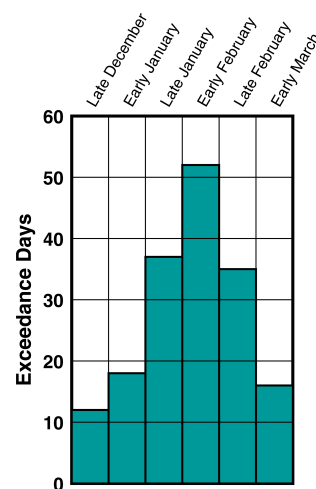
the season progresses, increasing and decreasing, respectively, the extents of the NO_x -sensitive and NO_x -saturation domains. Temperature and absolute humidity also drive the indicator curves upward, but their impact is smaller.

Secondly, the downward trend in NO_x concentration documented in Fig. 5 pushes typical concentration ranges (the black rectangles in Fig. 9) downward. In late December, the rectangle lies predominantly in the NO_x -saturation domain, while, in early March, it lies in the NO_x -sensitivity domain. This downward trend in NO_x concentration is probably the result of both dilution and emission effects. Dilution occurs because the typical mixing height increases with the passing season. Emissions change because there are processes and equipment linked to the temperature. Methane concentrations (and presumably, by extension, non-methane VOC concentrations) also decrease with the advancing season.

The results in Fig. 9 indicate that, all else being equal, ozone concentrations intensify as the season progresses. The calculation in Table 5 indicates that the solar zenith angle is the most important variable driving this increase.

On the basis of these results, we recommend that Uinta Basin ozone mitigation be focused on controlling both NO_x and VOC. NO_x controls in early winter could conceivably stimulate higher ozone (whenever $S_{NO_x} < 0$), but there are fewer daily exceedances then (Fig. 10) with lower ozone on average (Fig. 9), and any early-winter ozone increases will probably be more than offset by decreases in February and March.

As already mentioned, seasonal trends in the photochemical regime are very common throughout the Northern Hemisphere (Kleinman, 1991; Jacob et al., 1995; Liang et al., 1998; Martin et al., 2004; Jin et al., 2017). This study identifies the primary drivers for the trend in the Uinta Basin from late December to early March. No doubt these drivers have a similar effect elsewhere, but we should be cautious in extending these results to other regions. For example, biogenic emissions are probably a more important driver of seasonal trends in many regions than they are in the arid Uinta Basin. However, the fact that such trends are ubiquitous may derive from the fact that the actinic flux is the single most important driver in all regions.

**Figure 10.** The number of days in each of the 6 fortnights between December 2009 and March 2020 during which the 8 h average of ozone concentration at the Ouray monitoring station (central Uinta Basin) exceeded 70 ppb.

Code availability. F0AM code is available (see Mansfield and Lyman, 2025, <https://doi.org/10.5281/zenodo.17127373>).

Data availability. All observational data are available online (see USU BRC, 2025, <https://www.usu.edu/binghamresearch/data-access>).

Supplement. The supplement related to this article is available online at <https://doi.org/10.5194/acp-25-11261-2025-supplement>.

Author contributions. SNL compiled the observational data and developed the initial F0AM code. MLM ran the F0AM models, analyzed their results, and wrote the paper.

Competing interests. The contact author has declared that neither of the authors has any competing interests.

Disclaimer. Publisher's note: Copernicus Publications remains neutral with regard to jurisdictional claims made in the text, published maps, institutional affiliations, or any other geographical rep-

resentation in this paper. While Copernicus Publications makes every effort to include appropriate place names, the final responsibility lies with the authors.

Acknowledgements. Liji M. David, of Ramboll, performed the analysis of the OMI satellite data. Funding for this work was provided by the Utah State Legislature and Uintah Special Service District 1, Uintah County, Utah.

Review statement. This paper was edited by Steven Brown and reviewed by two anonymous referees.

References

- Ahmadov, R., McKeen, S., Trainer, M., Banta, R., Brewer, A., Brown, S., Edwards, P. M., de Gouw, J. A., Frost, G. J., Gilman, J., Helmig, D., Johnson, B., Karion, A., Koss, A., Langford, A., Lerner, B., Olson, J., Oltmans, S., Peischl, J., Pétron, G., Pichugina, Y., Roberts, J. M., Ryerson, T., Schnell, R., Senff, C., Sweeney, C., Thompson, C., Veres, P. R., Warneke, C., Wild, R., Williams, E. J., Yuan, B., and Zamora, R.: Understanding high wintertime ozone pollution events in an oil- and natural gas-producing region of the western US, *Atmos. Chem. Phys.*, 15, 411–429, <https://doi.org/10.5194/acp-15-411-2015>, 2015.
- Bishop, G. A., Haugen, M. J., McDonald, B. C., and Boies, A. M.: Utah Wintertime Measurements of Heavy-Duty Vehicle Nitrogen Oxide Emission Factors, *Environ. Sci. Technol.*, 56, 1885–1893, <https://doi.org/10.1021/acs.est.1c06428>, 2022.
- Choi, Y., Kim, H., Tong, D., and Lee, P.: Summertime weekly cycles of observed and modeled NO_x and O_3 concentrations as a function of satellite-derived ozone production sensitivity and land use types over the Continental United States, *Atmos. Chem. Phys.*, 12, 6291–6307, <https://doi.org/10.5194/acp-12-6291-2012>, 2012.
- Chou, C. C.-K., Tsai, C.-Y., Shiu, C.-J., Liu, S. C., and Zhu, T.: Measurement of NO_y during Campaign of Air Quality Research in Beijing 2006 (CAREBeijing-2006): Implications for the ozone production efficiency of NO_x , *J. Geophys. Res.*, 114, D00G01, <https://doi.org/10.1029/2008JD010446>, 2009.
- Dardiotis, C., Martini, G., Marotta, A., and Manfredi, U.: Low-temperature cold-start gaseous emissions of late technology passenger cars, *Appl. Energ.*, 111, 468–478, <https://doi.org/10.1016/j.apenergy.2013.04.093>, 2013.
- Duncan, B. N., Yoshida, Y., Olson, J. R., Sillman, S., Martin, R. V., Lamsal, L., Hu, Y., Pickering, K. E., Retscher, C., Allen, D. J., and Crawford, J. H.: Application of OMI observations to a space-based indicator of NO_x and VOC controls on surface ozone formation, *Atmos. Environ.*, 44, 2213–2223, <https://doi.org/10.1016/j.atmosenv.2010.03.010>, 2010.
- Edwards, P. M., Brown, S. S., Roberts, J. M., Ahmadov, R., Banta, R. M., deGouw, J. A., Dubé, W. P., Field, R. A., Flynn, J. H., Gilman, J. B., Graus, M., Helmig, D., Koss, A., Langford, A. O., Lefer, B. L., Lerner, B. M., Li, R., Li, S.-M., McKeen, S. A., Murphy, S. M., Parish, D. D., Senff, C. J., Soltis, J., Stutz, J., Sweeney, C., Thompson, C. R., Trainer, M. K., Tsai, C., Veres, P. R., Washenfelder, R. A., Warneke, C., Wild, R. J., Young, C. J., Yuan, B., and Zamora, R.: High winter ozone pollution from carbonyl photolysis in an oil and gas basin, *Nature*, 514, 351–354, <https://doi.org/10.1038/nature13767>, 2014.
- Finlayson-Pitts, B. J. and Pitts Jr., J. N.: *Chemistry of the Upper and Lower Atmosphere*, Academic Press, San Diego, ISBN 978-0-12-257060-5, 2000.
- Grange, S. K., Farren, N. J., Vaughan, A. R., Rose, R. A., and Carslaw, D. C.: Strong Temperature Dependence for Light-Duty Diesel Vehicle NO_x Emissions, *Environ. Sci. Technol.*, 53, 6587–6596, <https://doi.org/10.1021/acs.est.9b01024>, 2019.
- Hall, D. L., Anderson, D. C., Martin, C. R., Ren, X., Salawitch, R. J., He, H., Canty, T. P., Hains, J. C., and Dickerson, R. R.: Using near-road observations of CO, NO_y , and CO_2 to investigate emissions from vehicles: Evidence for an impact of ambient temperature and specific humidity, *Atmos. Environ.*, 232, 117558, <https://doi.org/10.1016/j.atmosenv.2020.117558>, 2020.
- Jacob, D. J., Horowitz, L. W., Munger, J. W., Heikes, B. G., Dickerson, R. R., Artz, R. S., and Keene, W. C.: Seasonal transition from NO_x - to hydrocarbon-limited conditions for ozone production over the eastern United States in September, *J. Geophys. Res.*, 100, 9315–9324, <https://doi.org/10.1029/94JD03125>, 1995.
- Jenkin, M. E., Saunders, S. M., Wagner, V., and Pilling, M. J.: Protocol for the development of the Master Chemical Mechanism, MCM v3 (Part B): tropospheric degradation of aromatic volatile organic compounds, *Atmos. Chem. Phys.*, 3, 181–193, <https://doi.org/10.5194/acp-3-181-2003>, 2003.
- Jenkin, M. E., Young, J. C., and Rickard, A. R.: The MCM v3.3.1 degradation scheme for isoprene, *Atmos. Chem. Phys.*, 15, 11433–11459, <https://doi.org/10.5194/acp-15-11433-2015>, 2015.
- Jin, X., Fiore, A. M., Murray, L. T., Valin, L. C., Lamsal, L. N., Duncan, B., Boersma, K. F., De Smedt, I., Gonzalez Abad, G., Chance, K., and Tonnesen, G. S.: Evaluating a Space-Based Indicator of Surface Ozone- NO_x -VOC Sensitivity Over Midlatitude Source Regions and Application to Decadal Trends, *J. Geophys. Res.-Atmos.*, 122, 10439–10491, <https://doi.org/10.1002/2017JD026720>, 2017.
- Kendall, M. G.: *Rank Correlation Methods*, 4th edn., London, Griffin, ISBN 978-0-85-264199-6, 1975.
- Kerry, K. E. and Hawick, K. A.: Kriging interpolation on high-performance computers, in: *High Performance Computing and Networking, HPCN-Europe*, edited by: Sloot, P., Bubak, M., and Hertzberger, B., Lecture Notes in Computer Science, vol. 1401, Springer, Berlin, <https://doi.org/10.1007/BFb0037170>, 1998.
- Kleinman, L. I.: Seasonal Dependence of Boundary Layer Peroxide Concentration: The Low and High NO_x Regimes, *J. Geophys. Res.*, 96, 20721–20733, <https://doi.org/10.1029/91JD02040>, 1991.
- Largerion, Y. and Staquet, C.: Persistent inversion dynamics and wintertime PM_{10} air pollution in Alpine valleys, *Atmos. Environ.*, 135, 92–108, <https://doi.org/10.1016/j.atmosenv.2016.03.045>, 2016.
- Li, K., Jacob, D. J., Liao, H., Qiu, Y., Shen, L., Zhai, S., Bates, K. H., Sulprizio, M. P., Song, S., Lu, X., Zhang, Q., Zheng, B., Zhang, Y., Zhang, J., Lee, H. C., and Kuk, S. K.: Ozone pollution in the North China Plain spreading into the late-winter haze season, *P. Natl. Acad. Sci. USA*, 118, e2015797118, <https://doi.org/10.1073/pnas.2015797118>, 2021.

- Li, X., Dallmann, T. R., May, A. A., and Presto, A. A.: Seasonal and Long-Term Trend of on-Road Gasoline and Diesel Vehicle Emission Factors Measured in Traffic Tunnels, *Appl. Sci.-Basel*, 10, 2458, <https://doi.org/10.3390/app10072458>, 2020.
- Liang, J., Horowitz, L. W., Jacob, D. J., Wang, Y., Fiore, A. M., Logan, J. A., Gardner, G. M., and Munger, J. W.: Seasonal budgets of reactive nitrogen species and ozone over the United States, and export fluxes to the global atmosphere, *J. Geophys. Res.*, 103, 13435–13450, <https://doi.org/10.1029/97JD03126>, 1998.
- Lyman, S., Mansfield, M., and Shorthill, H.: Final Report: Uintah Basin Winter Ozone & Air Quality Study, 23–31, <https://www.usu.edu/binghamresearch/files/2013-final-report-uimssd-R.pdf> (last access: 2025), 2013.
- Lyman, S., Mansfield, M., Tran, H., and Tran, T.: Annual Report: Uinta Basin Air Quality Research, 33–35, <https://www.usu.edu/binghamresearch/files/reports/UBAQR-2018-AnnualReport.pdf> (last access: 2025), 2018.
- Lyman, S. N., Holmes, M., Tran, H., Tran, T., and O'Neil, T.: High ethylene and propylene in an area dominated by oil production, *Atmosphere-Basel*, 12, 1, <https://doi.org/10.3390/atmos12010001>, 2021.
- Lyman, S. N., Elgiar, T., Gustin, M. S., Dunham-Cheatham, S. M., David, L. M., and Zhang, L.: Evidence against Rapid Mercury Oxidation in Photochemical Smog, *Environ. Sci. Technol.*, 56, 11225–11235, 2022.
- Mann, H. B.: Nonparametric tests against trend, *Econometrica*, 13, 245–259, <https://doi.org/10.2307/1907187>, 1945.
- Mansfield, M. L. and Hall, C. F.: Statistical analysis of winter ozone events, *Air Qual. Atmos. Hlth.*, 6, 687–699, <https://doi.org/10.1007/s11869-013-0204-0>, 2013.
- Mansfield, M. L. and Hall, C. F.: A survey of valleys and basins of the western United States for the capacity to produce winter ozone, *J. Air Waste Manage.*, 68, 909–919, <https://doi.org/10.1080/10962247.2018.1454356>, 2018.
- Mansfield, M. L. and Lyman, S. N.: Winter Ozone Pollution in Utah's Uinta Basin is Attenuating, *Atmosphere-Basel*, 12, 4, <https://doi.org/10.3390/atmos12010004>, 2021.
- Mansfield, M. and Lyman, S.: FOAM model script for Horsepool, Utah, wintertime ozone formation, Zenodo [code], <https://doi.org/10.5281/zenodo.17127373>, 2025.
- Martin, R. V., Fiore, A. M., and Van Donkelaar, A.: Space-based diagnosis of surface ozone sensitivity to anthropogenic emissions, *Geophys. Res. Lett.*, 31, L06120, <https://doi.org/10.1029/2004GL019416>, 2004.
- Matichuk, R., Tonnesen, G., Luecken, D., Gilliam, R., Napelenok, S. L., Baker, K. R., Schwede, D., Murphy, B., Helmig, D., Lyman, S., and Roselle, S.: Evaluation of the Community Multi-scale Air Quality Model for Simulating Winter Ozone Formation in the Uinta Basin, *J. Geophys. Res.-Atmos.*, 122, 13545–13572, <https://doi.org/10.1002/2017JD027057>, 2017.
- Mazzuca, G. M., Ren, X., Loughner, C. P., Estes, M., Crawford, J. H., Pickering, K. E., Weinheimer, A. J., and Dickerson, R. R.: Ozone production and its sensitivity to NO_x and VOCs: results from the DISCOVER-AQ field experiment, Houston 2013, *Atmos. Chem. Phys.*, 16, 14463–14474, <https://doi.org/10.5194/acp-16-14463-2016>, 2016.
- MCM: The Master Chemical Mechanism, <http://mcm.york.ac.uk/>, last access: February 2022.
- NASA Giovanni: <https://giovanni.gsfc.nasa.gov/giovanni/> (last access: September 2024), 2022.
- NASA OMI: <https://www.earthdata.nasa.gov/learn/find-data/near-real-time/omi>, last access: September 2022.
- NOAA GML: https://gml.noaa.gov/ccgg/trends_ch4/, last access: September 2022.
- Peng, Y. P., Chen, Y. S., Wang, H. K., and Lai, C. H.: In Situ Measurements of Hydrogen Peroxide, Nitric Acid and Reactive Nitrogen to Assess the Ozone Sensitivity in Pingtung County, Taiwan, *Aerosol Air Qual. Res.*, 11, 59–69, <https://doi.org/10.4209/aaqr.2010.10.0091>, 2011.
- Reiter, M. S. and Kockelman, K. M.: The problem of cold starts: A closer look at mobile source emission levels, *Transport Res. D-Tr. E.*, 43, 123–132, <https://doi.org/10.1016/j.trd.2015.12.012>, 2016.
- Rickard, A. R., Salisbury, G., Monks, P. S., Lewis, A. C., Baugitte, S., Bandy, B. J., Clemitshaw, K. C., and Penkett, S. A.: Comparison of Measured Ozone Production Efficiencies in the Marine Boundary Layer at Two European Coastal Sites under Different Pollution Regimes, *J. Atmos. Chem.*, 43, 107–134, <https://doi.org/10.1023/A:1019970123228>, 2002.
- Saha, P. K., Khlystov, A., Snyder, M. G., and Grieshop, A. P.: Characterization of air pollutant concentrations, fleet emission factors, and dispersion near a North Carolina interstate freeway across two seasons, *Atmos. Environ.*, 177, 143–153, <https://doi.org/10.1016/j.atmosenv.2018.01.019>, 2018.
- Saunders, S. M., Jenkin, M. E., Derwent, R. G., and Pilling, M. J.: Protocol for the development of the Master Chemical Mechanism, MCM v3 (Part A): tropospheric degradation of non-aromatic volatile organic compounds, *Atmos. Chem. Phys.*, 3, 161–180, <https://doi.org/10.5194/acp-3-161-2003>, 2003.
- Schnell, R. C., Oltmans, S. J., Neely, R. R., Endres, M. S., Molnar, J. V., and White, A. B.: Rapid photochemical production of ozone at high concentrations in a rural site during winter, *Nat. Geosci.*, 2, 120, <https://doi.org/10.1038/ngeo415>, 2009.
- Seinfeld, J. H. and Pandis, S. N.: *Atmospheric Chemistry and Physics: From Air Pollution to Climate Change*, 2nd edn., Wiley, 2006. See pp. 215 ff for a discussion of ozone production efficiency; p. 765 for the formula to calculate the saturation vapor pressure of water, ISBN 978-1-11-859136-9, 2006.
- Shah, V., Jacob, D. J., Li, K., Silvern, R. F., Zhai, S., Liu, M., Lin, J., and Zhang, Q.: Effect of changing NO_x lifetime on the seasonality and long-term trends of satellite-observed tropospheric NO₂ columns over China, *Atmos. Chem. Phys.*, 20, 1483–1495, <https://doi.org/10.5194/acp-20-1483-2020>, 2020.
- Sillman, S.: The use of NO_y, H₂O₂, and HNO₃ as indicators for ozone-NO_x-hydrocarbon sensitivity in urban locations, *J. Geophys. Res.*, 100, 14175–14188, <https://doi.org/10.1029/94JD02953>, 1995.
- Sillman, S.: The relation between ozone, NO_x and hydrocarbons in urban and polluted rural environments, *Atmos. Environ.*, 33, 1821–1845, [https://doi.org/10.1016/S1352-2310\(98\)00345-8](https://doi.org/10.1016/S1352-2310(98)00345-8), 1999.
- Sillman, S., He, D., Cardelino, C., and Imhoff, R. E.: The Use of Photochemical Indicators to Evaluate Ozone-NO_x-Hydrocarbon Sensitivity: Case Studies from Atlanta, New York, and Los Angeles, *J. Air Waste Manage.*, 47, 1030–1040, <https://doi.org/10.1080/10962247.1997.11877500>, 1997.

- Sillman, S., He, D., Pippin, M. R., Daum, P. H., Imre, D. G., Kleinman, L. I., Lee, J. H., and Weinstein-Lloyd, J.: Model correlations for ozone, reactive nitrogen, and peroxides for Nashville in comparison with measurements: Implications for O_3 - NO_x -hydrocarbon chemistry, *J. Geophys. Res.*, 103, 22629–22644, <https://doi.org/10.1029/98JD00347>, 1998.
- Sillman, S. and He, D.: Some theoretical results concerning O_3 - NO_x -VOC chemistry and NO_x -VOC indicators, *J. Geophys. Res.*, 107, 4659, <https://doi.org/10.1029/2001JD001123>, 2002.
- Suarez-Bertoa, R. and Astorga, C.: Impact of cold temperature on Euro 6 passenger car emissions, *Environ. Pollut.*, 234, 318–329, <https://doi.org/10.1016/j.envpol.2017.10.096>, 2018.
- Tonnesen, G. S. and Dennis, R. L.: Analysis of radical propagation efficiency to assess ozone sensitivity to hydrocarbons and NO_x : 2. Long-lived species as indicators of ozone concentration sensitivity, *J. Geophys. Res.*, 105, 9227–9241, <https://doi.org/10.1029/1999JD900372>, 2000.
- USU BRC: Data Access, <https://www.usu.edu/binghamresearch/data-access>, last access: 23 September 2025.
- Wang, L., Wang, J., Tan, X., and Fang, C.: Analysis of NO_x Pollution Characteristics in the Atmospheric Environment in Changchun City, *Atmosphere-Basel*, 11, 30, <https://doi.org/10.3390/atmos11010030>, 2020.
- Wærsted, E. G., Sundvor, I., Denby, B. R., and Mu, Q.: Quantification of temperature dependence of NO_x emissions from road traffic in Norway using air quality modeling and monitoring data, *Atmos. Environ.*, 13, 100160, <https://doi.org/10.1016/j.aeaoa.2022.100160>, 2022.
- Weber, C., Sundvor, I., and Figenbaum, E.: Comparison of regulated emission factors of Euro 6 LDV in Nordic temperatures and cold start conditions: Diesel- and gasoline direct-injection, *Atmos. Environ.*, 206, 208–217, <https://doi.org/10.1016/j.atmosenv.2019.02.031>, 2019.
- Whiteman, C. D., Eisenbach, S., Pospichal, B., and Steinacker, R.: Comparison of Vertical Soundings and Sidewall Air Temperature Measurements in a Small Alpine Basin, *J. Appl. Meteorol. Clim.*, 43, 1635–1647, <https://doi.org/10.1175/JAM2168.1>, 2004.
- Wolfe, G. M., Marvin, M. R., Roberts, S. J., Travis, K. R., and Liao, J.: The Framework for 0-D Atmospheric Modeling (F0AM) v3.1, *Geosci. Model Dev.*, 9, 3309–3319, <https://doi.org/10.5194/gmd-9-3309-2016>, 2016.
- Zong, R., Xue, L., Wang, T., and Wang, W.: Inter-comparison of the Regional Atmospheric Chemistry Mechanism (RACM2) and Master Chemical Mechanism (MCM) on the simulation of acetaldehyde, *Atmos. Environ.*, 186, 144–149, <https://doi.org/10.1016/j.atmosenv.2018.05.013>, 2018.